

# Leveraging the RETFound foundation model for optic disc segmentation in retinal images

Zhenyi Zhao, Muthu Rama Krishnan Mookiah, Emanuele Trucco

VAMPIRE project,  
Computing, School of Science and Engineering  
University of Dundee  
Dundee, UK

Corresponding author: Zhenyi Zhao, 2578745@dundee.ac.uk

## Abstract

RETFound is a well-known foundation model (FM) developed for fundus camera and optical coherence tomography images. It has shown promising performance across multiple datasets in diagnosing diseases, both eye-specific and systemic, from retinal images. However, to our best knowledge, it has not been used for other tasks. We present the first adaptation of RETFound for optic disc segmentation, a ubiquitous and foundational task in retinal image analysis. The resulting segmentation system outperforms state-of-the-art, segmentation-specific baseline networks after training a head with only a very modest number of task-specific examples. We report and discuss results with four public datasets, IDRID, Drishti-GS, RIM-ONE-r3, and REFUGE, and a private dataset, GoDARTS, achieving about 96% Dice consistently across all datasets. Overall, our method obtains excellent performance in internal verification, domain generalization and domain adaptation, and exceeds most of the state-of-the-art baseline results. We discuss the results in the framework of the debate about FMs as alternatives to task-specific architectures. The code is available at: [link to be added after the paper is accepted]

## 1. Introduction

RETFound [1] is recognized as the first foundation model (FM) built from a large collection of retinal fundus camera and optical coherence tomography (OCT) images. It was demonstrated on classification tasks, i.e., diagnosing retinal and systemic diseases from retinal images. To our best knowledge, we present the first adaptation of RETFound for a substantially different task, namely optic disc (OD) segmentation in fundus camera images. We compared results against state-of-the-art, segmentation-specific architectures, finding that our RETFound-based system outperforms baseline networks after training a head with only a very modest number of task-specific examples. We comment on these results in the discussion section.

Changes in the appearance of anatomical structures of the retina observed in colour fundus photography, mainly OD, optic cup, fovea and above all retinal vessels, have been identified as a promising source of biomarkers for systemic diseases [2-17]. Segmenting such structures accurately is essential for retinal biomarkers research.

Supervised Convolutional Neural Network (CNN) models have shown strong performance in retinal image segmentation [2, 9-15, 17]. However, at least three limitations remain. First, unlike natural images, medical images require expert clinicians to be annotated, a notoriously labour-intensive and expensive task. For this reason, many medical image repositories remain unlabelled and unexploited. Second, the performance of supervised CNN models decreases rapidly when tested on datasets different from the ones used for training, and domain generalization methods proposed recently [3, 18-20] need large amounts of data. Third, almost all the supervised CNN models implement data augmentation. Augmentation techniques are either basic transformations, or generate completely new synthetic images (i.e., not modifications of existing ones). The former does not add much new information; the latter does,

but AI systems trained on image collections containing *completely* synthetic images (phantoms) are trusted less by clinicians than ones trained only or mostly with real images [21, 22].

FM have been introduced recently [1, 23-30] and addressed the problems above. FM are normally trained on very large volumes of unlabelled data using self-supervised learning (SSL) in order to generate a latent representation of the image domain. The representation is then used to perform specific downstream tasks after training a head with limited amount of task-specific labelled data [24]. An at-a-glance comparison of this paradigm with traditional, task-specific supervised learning models is shown in Figure 1.

RETFound is based on masked autoencoders (MAE) [25], a well-known SSL technology demonstrated on natural images with the ImageNet-1K dataset [31]. The MAE encoder is built in RETFound as the pre-trained encoder. Two independent RETFound models were trained on 904,170 fundus camera images and 736,442 OCT images [1]. As proven independently by RETFound and other FM work [25-30], FMs address the limitations of supervised CNN models: first, unlabelled data are used effectively; second, generalization is improved significantly [1, 24, 25]; third, RETFound, trained fully on real retinal images with only basic geometric augmentations, is more acceptable to clinicians than systems relying on augmentation by totally synthetic phantoms.

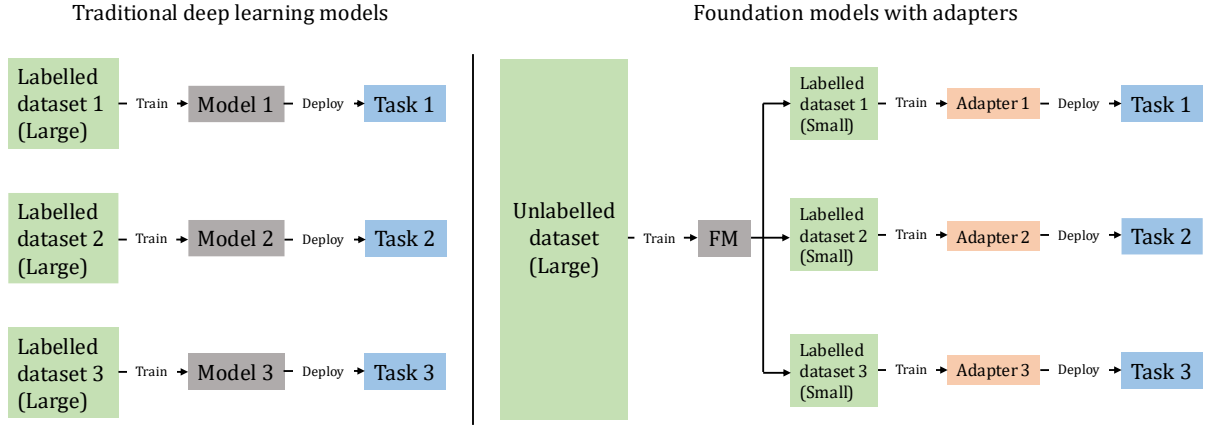


Figure 1. Differences between traditional deep learning models (left) and foundation models with adapters (right).

To our best knowledge, RETFound has not yet been adapted to the task of segmenting retinal anatomical structures in fundus camera images, which we explore for the specific task of OD segmentation in fundus camera images. This well-known task targets a clear and compact structure (unlike the vasculature), and allows us to compare results with those of several state-of-the-art systems. We adopt the encoder of RETFound as the pre-trained encoder, and the decoder of Segmenter [32] as the segmentation head. We train the model head with annotated images from a local dataset (GoDARTS [33]) and four public datasets (IDR1D [4], Drishti-GS [5], RIM-ONE-r3 [6], REFUGE [7]). We compare performance with two state-of-the-art baseline systems: VAMPIRE’s DUNet [2] and a benchmark domain generalization model for OD segmentation, DOFE [3].

In summary, the contributions of this paper are as follows.

1. To our best knowledge, using RETFound for retinal image segmentation for the first time.
2. Achieving better performance than two state-of-the-art baseline networks on GoDARTS, and better or comparable performance on public datasets but with much smaller task-specific training sets.
3. Achieving state-of-the-art performance compared to task-specific networks designed for domain generalization, again with a small task-specific training set.

In the rest of the paper, we describe our methods in Section 2 and datasets and experimental details in Section 3. We present and discuss results in Section 4 and 5 and our conclusions in Section 6.

## 2. Methods

### 2.1. Model architecture

We adapted Segmenter's decoder [32] to be used with RETFound. Figure 2 presents the architecture of our model.

#### 2.1.1. RETFound summary

To summarize the description in [1], RETFound uses the large vision Transformer, ViT-large [34], with 24 Transformer blocks as the encoder part. The embedding vector size is 1024 and the number of multi-head attention is 16. The unlabelled input retinal images are split into patches with a size of  $16 \times 16$ , and projected into a feature vector with a size of 1024. The positions of all features are embedded. ViT-large takes these feature vectors as input and generate high-level features. A decoder is added to the encoder for self-supervised learning. After completing self-supervised learning, RETFound has learnt rich hidden information from the unlabelled input retinal images. Then the decoder is removed and a Multi-Layer Perceptron (MLP) layer is adapted to the encoder for classification tasks. Also, a class token is added as image representation for providing class prediction after MLP layer.

#### 2.1.2. Our method

In our work, we froze the weights of RETFound, and removed the MLP layer and the class token, so that we can use RETFound to extract high-level features from any retinal datasets. Then we adapted the decoder of Segmenter to work with RETFound. The decoder contains a Mask Transformer block, including two Transformer blocks with the embedding vector size of 1024 and the number of multi-head attention set to 16. New class tokens for masks are added, and the number of class tokens equals the number of mask classes. The Mask Transformer takes the high-level features from RETFound and generates new feature vectors. Mask maps are obtained by scalar product of class tokens and feature vectors. Each mask sequence is bilinearly upsampled to the original image size to obtain a feature map, then softmax is used to calculate class scores to generate the final segmentation map.

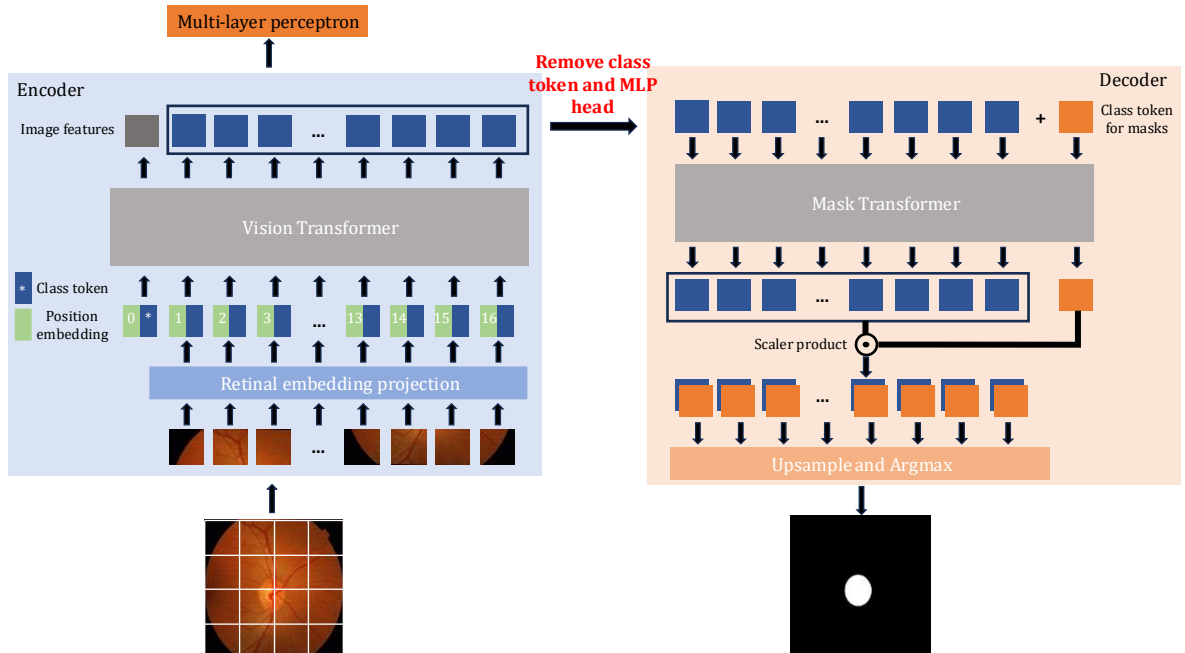


Figure 2. Model architecture of our method. Left: the encoder from RETFound. We froze the weights of RETFound, and remove the multi-layer perceptron head and the class token. Right: the decoder from Segmenter, that we adapted. We used the values from truncated normal distribution to initialize the weights.

## 2.2. Loss functions

The cross-entropy loss is used in Segmenter as the loss function for segmentation tasks. However, we find that use a combination of Dice loss and Binary Cross Entropy loss (BCELoss) can achieve better performance and faster model convergence speed (details in Section 5.2). The definition of Dice loss is:

$$L_{Dice} = 1 - \frac{2TP}{2TP + FP + FN}, \quad (1)$$

where  $TP$  is true positive,  $FP$  is false positive, and  $FN$  is false negative. The definition of BCELoss is:

$$L_{BCE} = -\frac{1}{n} \sum_{i=1}^n [y_i \log \hat{y}_i + (1 - y_i) \log(1 - \hat{y}_i)], \quad (2)$$

where  $n$  is the number of samples,  $y$  is the ground truth segmentation label (figure or background), and  $\hat{y}$  is the predicted label. So, the total loss function is:

$$L_{Total} = L_{Dice} + L_{BCE}. \quad (3)$$

## 3. Experiments design and datasets

### 3.1. Experiment settings

In order to evaluate the potential of using RETFound for OD segmentation in fundus camera images, especially its generalization performance, we designed three experiments, aimed respectively at *internal verification*, *domain generalization* and *domain adaptation*. Implementation details are given in Section 3.4.

*Internal verification:* We divided each dataset used (independently) in training / validation and testing subsets, and used the subsets as customary.

*Domain generalization:* Following the experimental design of DOFE [3], one of our baselines, we trained the model using all images from three of the four training sets simultaneously; we then tested performance on the testing set of the fourth dataset, unused for training, and repeated the experiments for each dataset as testing dataset.

*Domain adaptation:* We trained the model on the training set of each dataset, one at a time, and tested performance on the testing sets of all the other datasets.

In addition, we evaluated the effectiveness of RETFound for OD segmentation by comparing results obtained with three data augmentation strategies. First, we did not apply any data augmentation; images were just resized to  $224 \times 224$ , followed by Z-score normalization. Second, we applied two basic spatial-level augmentations, namely random rotate and flipping. Third, we used deep stacked transformations (DST) [35], a stack of augmentations designed for medical images. This includes random sharpening, blurring, noise, brightness adjustment, contrast change, perturbation, rotation, and deformation. Note that the original DST includes cropping and resizing, but cropping caused performance to decrease in our experiments (Table 1).

Dataset	Augmentation	Dice results (%)
GoDARTS	Unaugmented	94.14
GoDARTS	Spatial (with cropping)	88.52

GoDARTS	DST (with cropping)	86.87
---------	---------------------	-------

Table 1. Initial experiment results for augmentation selection. All the other settings are the same.

### 3.2. Datasets

Table 2 lists the datasets and their splits in our experiments. We randomly partition all the training sets into training and validation sets based on a ratio of 4:1, except REFUGE which contain the independent validation set. Following the distribution analysis design of DOFE [3], we utilized t-SNE [36] to visualise the distribution of image features extracted from all the datasets by VGG16 [37] pretrained on ImageNet [31]. The visualization results are shown in Figure 3; different datasets are colour coded. Training and testing set in each datasets have similar distributions, except for REFUGE. The distributions of all the datasets are quite different from each other, only some of the images from GoDARTS and IDRID, and a few of training samples from Drishti-GS have similar distributions (Figure 3 Left). However, the distributions of designed domain datasets are much separated from each other (Figure 3 Right).

Task	Datasets	Number of images		Number of annotators	Ways to solve disagreement	Annotators	Automation
		Training	Testing				
<i>Internal verification and domain adaptation</i>	GoDARTS [33]	201	25	1	-	Retinal specialists	Semi-automatic
	IDRID [4]	54	27	2	Discussion	Retinal specialists	Semi-automatic
	Drishti-GS [5]	50	51	4	Agreement from 3 experts	Glaucoma experts	Manual
	RIM-ONE-r3 [6]	99	60	5	Average	4 Ophthalmologists and 1 optometrist	Manual
	REFUGE [7]	800	400	7	Majority voting	Glaucoma specialists	Manual
<i>Domain generalization</i>	Drishti-GS (Domain 1)	50	51	-	-	-	-
	RIM-ONE-r3 (Domain 2)	99	60	-	-	-	-
	REFUGE (train) (Domain 3)	320	80	-	-	-	-
	REFUGE (validation) (Domain 4)	320	80	-	-	-	-

Table 2. OD segmentation datasets, annotation characteristics and splits, defining the domains used in the main text. Note the very small number of segmentation-specific training images compared to those used by the baseline segmentation-specific networks (details in Table 7).

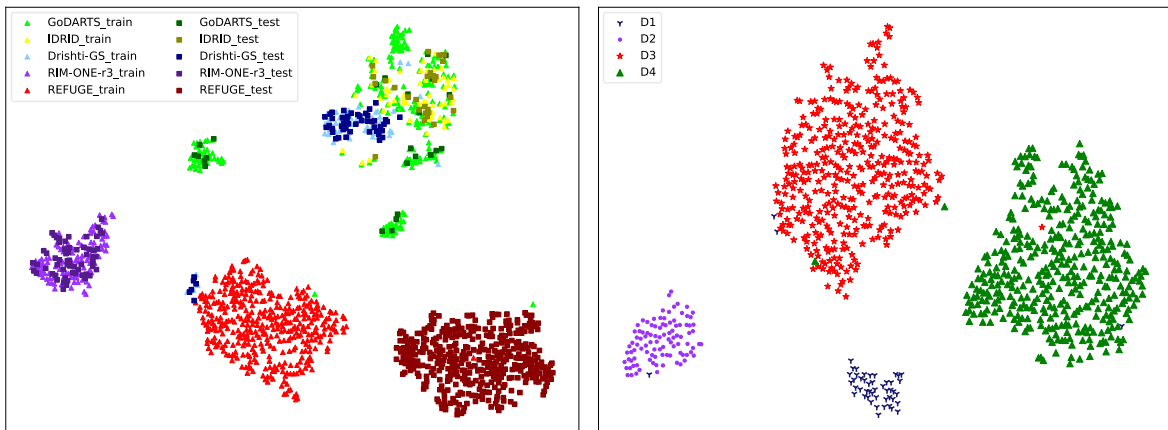


Figure 3. Left: t-SNE visualization of image feature clusters from training sets and testing sets of the datasets used. Right: same but for the four domain datasets defined in Table 2. D1, D2, D3 and D4 stand for Domain 1, ..., Domain 4.

### 3.3. Evaluation metrics

We adopt three metrics to evaluate the OD segmentation performance, namely Dice, 95% of the Hausdorff Distance (HD), and Average Surface Distance (ASD). The definition of Dice is:

$$Dice = \frac{2TP}{2TP + FP + FN}, \quad (4)$$

where  $TP$  is true positive,  $FP$  is false positive, and  $FN$  is false negative. The definition of 95% HD is:

$$95\% HD = \max\{h(\hat{Y}, Y), h(Y, \hat{Y})\}, \quad (5)$$

where  $\hat{Y}$  and  $Y$  are the sets of points (pixels) of predictions and ground truth, and  $h(\hat{Y}, Y)$  and  $h(Y, \hat{Y})$  the Hausdorff distances from  $\hat{Y}$  to  $Y$  and  $Y$  to  $\hat{Y}$ , respectively, which are defined as:

$$h(\hat{Y}, Y) = 95\% \max_{i \in [1, n]} \left\{ \min_{j \in [1, n]} \{d(\hat{y}_i, y_j)\} \right\}, \quad (6)$$

$$h(Y, \hat{Y}) = 95\% \max_{j \in [1, n]} \left\{ \min_{i \in [1, n]} \{d(y_j, \hat{y}_i)\} \right\}, \quad (7)$$

where  $n$  is the number of points,  $\hat{y}$  and  $y$  points belonging to  $\hat{Y}$  and  $Y$ , respectively, and  $d$  is Euclidian distance (but could be other metrics depending on users).

The definition of ASD is:

$$ASD = \frac{1}{n} \sum_{i=1}^n \min_{j \in [1, n]} \{d(\hat{y}_i, y_j)\}, \quad (8)$$

where  $n$ ,  $\hat{y}$ ,  $y$  and  $d$  are defined as for the 95% HD metric.

### 3.4. Implementation details

All images are resized to  $224 \times 224$  by cubic interpolation, as done in RETFound [1]. As described in Section 3.1, three data augmentation strategies are applied, depending on the specific task, followed by Z-score normalization. 95% HD and ASD are sensitive to the number of correctly classified pixels, so we apply post-processing in the interest of a fair comparison for domain generalization: we resize the segmentation map to the original size by cubic interpolation, crop the  $800 \times 800$  area based on the centre of OD, and resize the map to the size of  $256 \times 256$  by cubic interpolation, which is the same as done in the pre-processing of DOFE [3] and other state-of-the-art methods for domain generalization [18-20]. The learning rate used is 0.001 and the batch size is 4. Note that we tried multiple learning rate strategies, including step decay, cosine decay with warmup and Cosine Annealing [38], but either the model failed to converge, or the performance degraded significantly (details in Section 5.1). Adam optimization is used for optimizing the weights. Epochs are set to 3,200,000 divided by the number of training images, an empirically determined figure giving enough training and best results (details in Section 5.1). The weights corresponding to the best performance during validation are saved as the final ones. All experiments were run on a commercial-grade desktop with a 12GB memory size NVIDIA TITAN XP GPU and a 3.2GHz Intel Core i7-8700 CPU under Ubuntu 16.04 system.

## 4. Results

The results of the internal verification and their comparisons with the baseline methods are given in Table 3. Domain generalization results are summarized in Table 4 to 6, and the domain adaptation results in Table 7. In all the result tables, bold identifies best performance, and underlining the second-best one.

The two baselines for comparing results are DOFE [3] and VAMPIRE’s DUNet [2]. DOFE was chosen as it is a commonly used baseline [18-20] for OD segmentation and domain generalization with retinal fundus images. DUNet is the segmentation system adopted in the VAMPIRE software system [8].

In internal verification comparisons, the state-of-the-art methods [9-17] were chosen as they are the latest methods for OD segmentation testing on the same public datasets as ours and using different kinds of model architectures, based on U-Net, VGG, EfficientNet and Transformers. The state-of-the-art methods for comparing domain generalization and domain adaptation results were chosen as they are the latest methods with the best performance among the papers we reviewed.

#### 4.1. Internal verification

Table 3 presents the results of the internal verification. The best Dice scores of our methods on GoDARTS, IDRID, Drishti-GS and RIM-ONE-r3 are 95.76%, 95.82%, 97.68% and 96.84%, respectively, which exceed the state-of-the-art methods' results, apart from the result on REFUGE (95.77%), which is just slightly below the best one.

Methods	Year	Model Summary	Datasets					Average
			GoDARTS	IDRID	Drishti-GS	RIM-ONE-r3	REFUGE	
Xie et al. [9]	2020	U-Net based	-	-	97.6	-	-	-
Bian et al. [10]	2020	U-Net cascade network	-	-	-	-	93.3	-
DUNet [2]	2021	Dense U-Net	90.39	-	-	-	-	-
Imtiaz et al. [11]	2021	VGG-based	-	-	94.9	-	-	-
Pachade et al. [12]	2021	EfficientNet-based	-	-	96.3	95.5	<u>96.2</u>	-
Yin et al. [13]	2021	U-Net and level set combination	-	-	96.2	-	-	-
Joshi et al. [14]	2022	U-Net based	-	-	97.4	96.2	-	-
Hervella et al. [15]	2022	U-Net based	-	-	97.2	-	95.9	-
Yi et al. [16]	2023	Transformer-based	-	-	97.6	-	<b>96.9</b>	-
W-Net[17]	2024	CNN-based W-Net	-	95.25	95.34	-	-	-
Ours (None)	2025	Fine-tuning of self-supervised vision transformer foundation model	<u>95.68</u>	95.26	<u>97.65</u>	<b>96.84</b>	95.77	<u>96.24</u>
Ours (Spatial)	2025		<b>95.76</b>	<b>95.82</b>	97.31	<u>96.81</u>	95.73	<b>96.29</b>
Ours (DST)	2025		95.31	<u>95.38</u>	<b>97.68</b>	96.41	95.69	96.09

Table 3. Results of our method leveraging RETFound compared with state-of-the-art baselines. All figures are Dice values (%). We could not find published results for the empty cells.

#### 4.2. Domain generalization

Table 4 to 6 present the results of our domain generalization experiments. Our method outperforms the state-of-the-art task-specific baselines throughout.

Metric: Dice (%)		Target domain				Average
Methods	Year	Domain 1	Domain 2	Domain 3	Domain 4	
DOFE [3]	2020	95.59	89.37	91.98	93.32	92.57
RAM [18]	2022	95.62	88.07	94.83	93.53	93.01
TVConv [19]	2022	95.56	92.73	93.58	93.63	93.87
DCAM-NET [20]	2023	<u>96.15</u>	92.02	93.95	93.93	94.01
Ours (None)	2025	95.97	92.15	<b>95.39</b>	95.15	94.67
Ours (Spatial)	2025	<u>96.15</u>	<b>94.92</b>	<u>95.37</u>	<b>95.68</b>	<b>95.53</b>
Ours (DST)	2025	<b>96.28</b>	<u>93.30</u>	95.13	<u>95.30</u>	<u>95.00</u>

Table 4. Results of our method leveraging RETFound compared with four recent domain generalization segmentation networks. All figures are Dice values (%).

Metric: 95% HD		Target domain				Average
Methods	Year	Domain 1	Domain 2	Domain 3	Domain 4	
DOFE [3]	2020	16.95	27.41	21.22	14.63	20.05
RAM [18]	2022	18.38	32.69	16.23	19.39	21.67
TVConv [19]	2022	16.57	20.51	17.70	16.26	17.76
DCAM-NET [20]	2023	15.69	21.78	17.77	15.14	17.59
Ours (None)	2025	7.16	10.54	<b>7.30</b>	<b>5.65</b>	<u>7.66</u>
Ours (Spatial)	2025	<b>6.94</b>	<b>7.56</b>	<u>7.84</u>	5.99	<b>7.08</b>
Ours (DST)	2025	<u>7.01</u>	<u>9.88</u>	8.61	<u>5.66</u>	7.79

Table 5. Results of our method leveraging RETFound compared with other latest domain generalization segmentation networks. All figures are 95% HD values.

Metric: ASD		Target domain				Average
Methods	Year	Domain 1	Domain 2	Domain 3	Domain 4	
DOFE [3]	2020	8.355	15.65	11.41	7.274	10.67
RAM [18]	2022	7.763	17.97	7.345	8.031	10.27
TVConv [19]	2022	7.675	10.72	9.021	8.115	8.882
DCAM-NET [20]	2023	6.80	11.39	8.564	7.437	8.547
Ours (None)	2025	2.23	4.09	<b>2.22</b>	1.73	2.57
Ours (Spatial)	2025	<u>2.16</u>	<b>2.52</b>	<u>2.34</u>	<b>1.64</b>	<b>2.17</b>
Ours (DST)	2025	<b>2.15</b>	<u>3.32</u>	2.50	<u>1.72</u>	<u>2.42</u>

Table 6. Results of our method leveraging RETFound compared with recent domain generalization segmentation networks. All figures are ASD values.

#### 4.3. Domain adaptation

Table 7 presents the results of domain adaptation experiments, the results of state-of-the-art domain adaptation methods, and the Dice result summary of domain generalization for comparisons. Our method obtains the best performance when testing on RIM-ONE-r3, and similar results to the state-of-the-art methods when testing on Drishti-GS.



Metric: Dice (%)	Source domain					Number of source domain images	Target domain		
Methods	IDRID	Drishti-GS	RIM-ONE-r3	REFUGE (Train)	REFUGE (Validation)		Drishti-GS	RIM-ONE-r3	REFUGE
DOFE [3]			✓	✓	✓	739	95.59	-	-
DOFE [3]		✓		✓	✓	690	-	89.37	-
RAM [18]			✓	✓	✓	739	95.62	-	-
RAM [18]		✓		✓	✓	690	-	88.07	-
TVConv [19]			✓	✓	✓	739	95.56	-	-
TVConv [19]		✓		✓	✓	690	-	92.73	-
DCAM-NET [20]			✓	✓	✓	739	96.15	-	-
DCAM-NET [20]		✓		✓	✓	690	-	92.02	-
S-CUDA [39]				✓		400	96.1	-	-
ISFA [40]				✓		400	96.6	90.8	-
ECSD-Net [41]				✓		400	96.5	86.5	-
RDR-Net [42]				✓		400	<b>97.1</b>	91.8	-
Ours (None)				✓		400	96.01	93.42	-
Ours (Spatial)				✓		400	95.82	92.27	-
Ours (DST)				✓		400	96.32	83.80	-
Ours (None)			✓			99	94.03	-	85.39
Ours (Spatial)			✓			99	94.64	-	84.55
Ours (DST)			✓			99	94.60	-	<u>91.72</u>
Ours (None)	✓					54	95.38	91.68	85.88
Ours (Spatial)	✓					54	<u>96.85</u>	94.08	88.86
Ours (DST)	✓					54	96.10	<u>94.60</u>	89.87
Ours (None)		✓				50	-	<b>94.68</b>	87.10
Ours (Spatial)		✓				50	-	94.45	87.50
Ours (DST)		✓				50	-	93.44	<b>93.54</b>

Table 7. Results of our method leveraging RETFound compared with recent domain adaptation segmentation networks, and a summary of recent domain generalization segmentation networks using Drishti-GS and RIM-ONE-r3 as target domains. All figures are Dice values (%). The ticks denote to the datasets used in each method, and the total number of training images are counted. We could not find results with REFUGE used as the target domain in the papers reviewed.

## 5. Discussion

### 5.1. Learning rate strategy selection and grokking

Most of the state-of-the-art methods use learning rate decay strategies [3, 10, 12, 13, 15-20, 32, 40-42, 43]. In our experiments, we use the fixed learning rate 0.001, which does not delay grokking [44], or delay generalization. Grokking means that generalization performance suddenly improves from random chance to near-perfect generalization levels before showing any generalization evidence (Figure 4). As Dosovitskiy *et al.* mentioned in the original ViT paper [34], Transformers need much larger datasets for training than CNNs. We found that using small datasets to train Transformers can still work when adapting Transformer blocks to a pre-trained FM, but grokking always appear. If the decay learning strategies are deployed, grokking will be delayed or never happen, which means the model will need much more epochs for training or the model will not converge within appropriate epochs (10,000 is the max number of epochs we tested). The reason for the unusually high number of epochs (10,000) instead of the common

hundreds is that Transformer blocks need more training on small datasets to make up for the lack of large datasets.

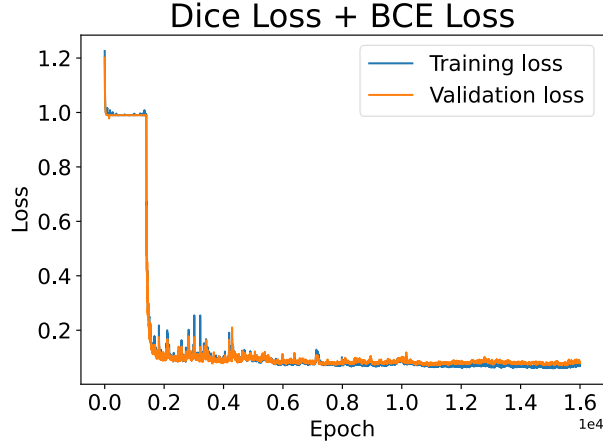


Figure 4. An example of grokking from our experiments. Generalization suddenly appears in training, here after about 1,800 epochs.

## 5.2. Loss function selection

As described in Section 2.2, we combine Dice loss and BCELoss in the loss function, unlike Segmenter (cross-entropy loss only). The advantage of BCELoss is that the accuracy of classification of each pixel is calculated independently, so the optimizer can set out on a promising convergence direction early on in training; instead, it is difficult for the Dice loss to begin to converge as it always considers a whole area. However, including correctly classified areas has benefits for edge processing and assuages the problem of foreground-background imbalance. In our case, OD segmentation is imbalanced segmentation as OD area is much smaller than the background. Therefore, using the combination of Dice loss and BCELoss can achieve both fast convergence and stable segmentation, as shown by the results of our initial experiments (Table 8).

<i>Dataset</i>	<i>Best result epoch</i>	<i>Loss function</i>	<i>Dice results (%)</i>
GoDARTS	14,080	BCELoss	93.41
GoDARTS	19,250	Dice loss	94.17
GoDARTS	12,186	BCELoss + Dice loss	94.14

Table 8. Initial experiment results for loss function selection. All the other settings are the same.

## 5.3. Internal verification analysis

Table 3 compared average results of the methods considered, showing that the models trained on datasets with DST augmentations obtain the worst results, although these are the most complex augmentations. This suggests that using RETFound focuses on image features most similar to those of the unaugmented images. A possible reason is that RETFound was trained on datasets with only basic augmentations including random crop, random horizontal flipping and resizing.

The average results from training data without augmentation and with basic spatial augmentation are quite close. This confirms that the original datasets can be used directly, provided that the distributions of training and testing sets are similar. Besides, models trained on GoDARTS (210 training images) and RIM-ONE-r3 (99 training images) *without* augmentation achieve the second-best and the best performance, respectively. In tests with DST augmentation, models trained on IDRID (54 training images) and Drishti-GS (50 training images) achieve the second-best and the

best performance, respectively. This confirms that larger training sets can support very good performance with simple augmentations, as expected.

When the training and testing sets have different distributions but were collected by the same device or organization (Figure 3), as in REFUGE, results with the model trained on training dataset without augmentation achieve the best Dice value (95.77%), compared to spatial augmentations (95.73%) and DST augmentations (95.69%). This suggests that slightly larger training dataset (e.g. 400 training images) *without* augmentation can potentially provide clinically acceptable performance when datasets are collected and used consistently within the same medical institution. This is an entirely plausible scenario, although mostly for high-resource clinical environment that can support training with large, local datasets.

In summary, our internal verification experiments support two conclusions. First, our system adapting RETFound to segment the OD in retinal fundus camera images achieves better or competitive results than our state-of-the-art baselines even though trained on very modest sets of task-specific images and with no augmentation. Second, basic spatial augmentations for fine-tuning RETFound for OD segmentation lead to better results than complex ones.

#### 5.4. Domain generalization and adaptation

In Table 4 to 6, again, basic spatial augmentations obtain the best performance. Similarly to what reported in Section 5.3, this suggests that fine-tuning RETFound still benefits from data augmentation in domain generalization problems for specific tasks, and basic spatial augmentations seem more effective than complex ones. Meanwhile, datasets *without* augmentations still achieve excellent comparative results.

In Table 7, the results indicate that RETFound supports strong generalization on the domain adaptation task, even when the source domain (RIM-ONE-r3, IDRID and Drishti-GS) and target domain (REFUGE) are very different, and the number of training images (99, 54 and 50) is much smaller than the number of testing images (400). We could not find any work reporting results of REFUGE as target domain; in any case, our results (93.54%) are rather close to state-of-the-art internal verification ones (96.9%), but DST augmentation is needed.

#### 5.5. Performance stability

Performance stability, defined as maintaining good performance in the presence of out-of-distribution images, is especially important in medical applications. Figure 5 shows the best result and the worst result of the models which achieve the best performance in all the three tasks we identified. The best segmentation results of all the models nearly overlap with the ground truth, indicating that our method has high accuracy. In internal verification, the worst results are visually still quite close to the ground truth, a situation occurring also in our domain generalization and domain adaptation experiments. However, some retinal areas were incorrectly classified as OD when using RIM-ONE-r3 and IDRID as source domain and REFUGE as target domain. This error only appeared in a single REFUGE test image (image 397), and the error areas are quite similar. This suggests that our method only make mistakes when the features of testing images were never observed at all in training.

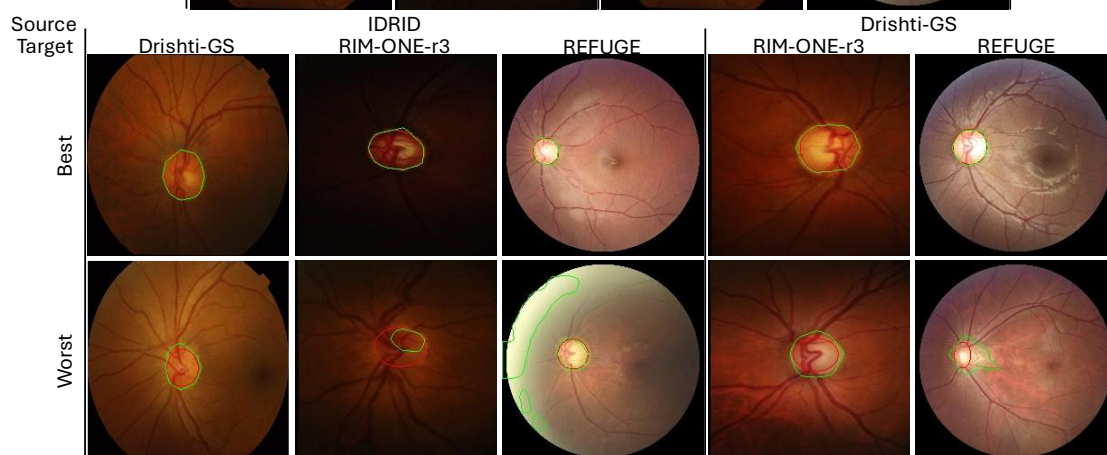
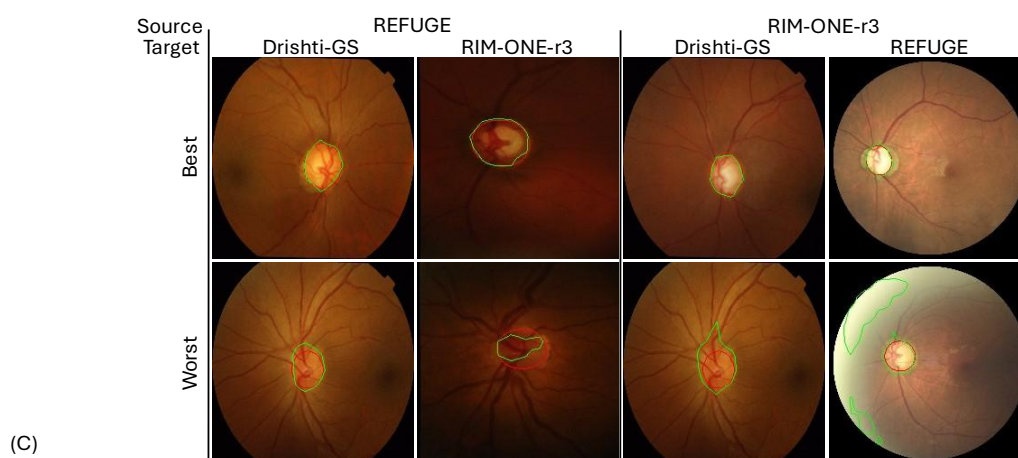
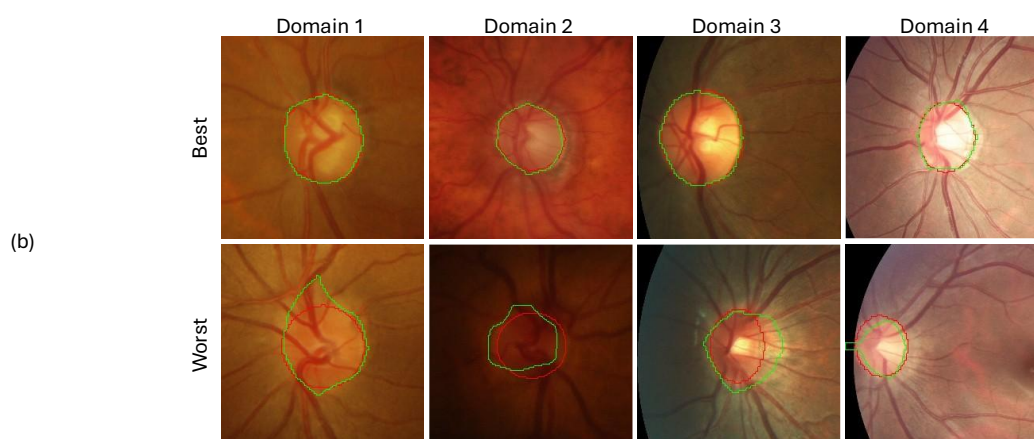
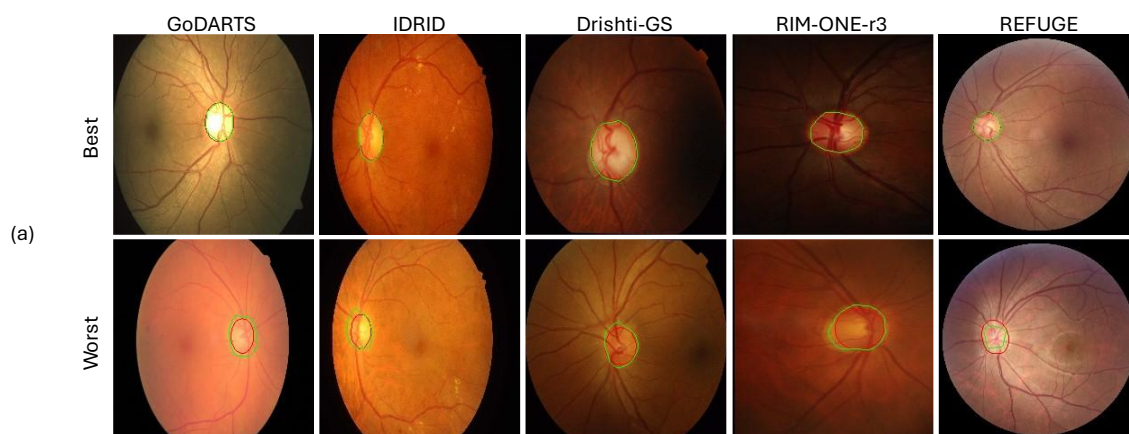


Figure 5. Best result and worst results of the models which achieve the best performance in all the three tasks. The red circle denotes to the ground truth, while the green circle is our segmentation results. (a) Internal verification results. (b) Domain generalization results. (c) Domain adaptation results.

## 6. Conclusion

This paper has presented, to our best knowledge, the first adaptation of the RETFound foundation model to a segmentation problem, as opposed to the classification ones reported in the original RETFound paper and other work [43, 45-46]. We used Segmenter's decoder to explore the potential of the general representation computed by RETFound for a fundamental task in retinal image analysis, namely segmenting the OD in fundus camera images.

The resulting segmentation model achieved high performance, surpassing nearly always that of state-of-the-art baseline methods in all the internal verification, domain adaptation and domain generalization experiments. Furthermore, the model showed similar (high) performance level in internal verification experiments without any data augmentation compared with experiments involving basic spatial data augmentation and complex DST augmentation.

Future work directions based on limitation of our current work exploring further, important tasks in retinal image analysis, like vessel segmentation and characterization, and discovering biomarkers for systemic conditions [47-49].

## References

- [1] Zhou, Y., Chia, M. A., Wagner, S. K., Ayhan, M. S., Williamson, D. J., Struyven, R. R., ... & Keane, P. A. (2023). A foundation model for generalizable disease detection from retinal images. *Nature*, 622(7981), 156-163.
- [2] Mookiah, M. R. K., Hogg, S., MacGillivray, T., & Trucco, E. (2021). On the quantitative effects of compression of retinal fundus images on morphometric vascular measurements in VAMPIRE. *Computer Methods and Programs in Biomedicine*, 202, 105969.
- [3] Wang, S., Yu, L., Li, K., Yang, X., Fu, C. W., & Heng, P. A. (2020). DOFE: Domain-oriented feature embedding for generalizable fundus image segmentation on unseen datasets. *IEEE Transactions on Medical Imaging*, 39(12), 4237-4248.
- [4] Porwal, P., Pachade, S., Kamble, R., Kokare, M., Deshmukh, G., Sahasrabudhe, V., & Meriaudeau, F. (2018). Indian diabetic retinopathy image dataset (IDRiD): a database for diabetic retinopathy screening research. *Data*, 3(3), 25.
- [5] Sivaswamy, J., Krishnadas, S., Chakravarty, A., Joshi, G., & Tabish, A. S. (2015). A comprehensive retinal image dataset for the assessment of glaucoma from the optic nerve head analysis. *JSM Biomedical Imaging Data Papers*, 2(1), 1004.
- [6] Fumero, F., Alayón, S., Sanchez, J. L., Sigut, J., & Gonzalez-Hernandez, M. (2011, June). RIM-ONE: An open retinal image database for optic nerve evaluation. In 2011 24th international symposium on computer-based medical systems (CBMS) (pp. 1-6). IEEE.
- [7] Orlando, J. I., Fu, H., Breda, J. B., Van Keer, K., Bathula, D. R., Diaz-Pinto, A., ... & Bogunović, H. (2020). Refuge challenge: A unified framework for evaluating automated methods for glaucoma assessment from fundus photographs. *Medical image analysis*, 59, 101570.
- [8] Perez-Rovira, A., MacGillivray, T., Trucco, E., Chin, K. S., Zutis, K., Lupascu, C., ... & Dhillon, B. (2011, August). VAMPIRE: Vessel assessment and measurement platform for images of the REtina. In 2011 Annual International Conference of the IEEE Engineering in Medicine and Biology Society (pp. 3391-3394). IEEE.
- [9] Xie Z, Ling T, Yang Y, Shu R, Liu BJ. Optic disc and cup image segmentation utilizing contour-based transformation and sequence labeling networks. *Journal of Medical Systems*. 2020 May;44:1-3.

- [10] Bian X, Luo X, Wang C, Liu W, Lin X. Optic disc and optic cup segmentation based on anatomy guided cascade network. *Computer Methods and Programs in Biomedicine*. 2020 Dec 1;197:105717.
- [11] Imtiaz R, Khan TM, Naqvi SS, Arsalan M, Nawaz SJ. Screening of glaucoma disease from retinal vessel images using semantic segmentation. *Computers & Electrical Engineering*. 2021 May 1;91:107036.
- [12] Pachade S, Porwal P, Kokare M, Giancardo L, Mériaudeau F. NENet: Nested EfficientNet and adversarial learning for joint optic disc and cup segmentation. *Medical Image Analysis*. 2021 Dec 1;74:102253.
- [13] Yin P, Xu Y, Zhu J, Liu J, Huang H, Wu Q. Deep level set learning for optic disc and cup segmentation. *Neurocomputing*. 2021 Nov 13;464:330-41.
- [14] Joshi A, Sharma KK. Graph deep network for optic disc and optic cup segmentation for glaucoma disease using retinal imaging. *Physical and Engineering Sciences in Medicine*. 2022 Sep;45(3):847-58.
- [15] Hervella, Á. S., Rouco, J., Novo, J., & Ortega, M. (2022). End-to-end multi-task learning for simultaneous optic disc and cup segmentation and glaucoma classification in eye fundus images. *Applied Soft Computing*, 116, 108347.
- [16] Yi, Y., Jiang, Y., Zhou, B., Zhang, N., Dai, J., Huang, X., ... & Zhou, W. (2023). C2FTFNet: Coarse-to-fine transformer network for joint optic disc and cup segmentation. *Computers in Biology and Medicine*, 164, 107215.
- [17] Tang, S., Song, C., Wang, D., Gao, Y., Liu, Y., & Lv, W. (2024). W-Net: A boundary-aware cascade network for robust and accurate optic disc segmentation. *Iscience*, 27(1).
- [18] Zhou, Z., Qi, L., & Shi, Y. (2022, October). Generalizable medical image segmentation via random amplitude mixup and domain-specific image restoration. In *European Conference on Computer Vision* (pp. 420-436). Cham: Springer Nature Switzerland.
- [19] Chen, J., He, T., Zhuo, W., Ma, L., Ha, S., & Chan, S. H. G. (2022). Tvconv: Efficient translation variant convolution for layout-aware visual processing. In *proceedings of the IEEE/CVF conference on computer vision and pattern recognition* (pp. 12548-12558).
- [20] Hua, K., Fang, X., Tang, Z., Cheng, Y., & Yu, Z. (2023). DCAM-NET: A novel domain generalization optic cup and optic disc segmentation pipeline with multi-region and multi-scale convolution attention mechanism. *Computers in Biology and Medicine*, 163, 107076.
- [21] Chen, J. S., Coyner, A. S., Chan, R. P., Hartnett, M. E., Moshfeghi, D. M., Owen, L. A., ... & Campbell, J. P. (2021). Deepfakes in ophthalmology: applications and realism of synthetic retinal images from generative adversarial networks. *Ophthalmology Science*, 1(4), 100079.
- [22] Veturi, Y. A., Woof, W., Lazebnik, T., Moghul, I., Woodward-Court, P., Wagner, S. K., ... & Pontikos, N. (2023). SynthEye: investigating the impact of synthetic data on artificial intelligence-assisted gene diagnosis of inherited retinal disease. *Ophthalmology Science*, 3(2), 100258.
- [23] Moor, M., Banerjee, O., Abad, Z. S. H., Krumholz, H. M., Leskovec, J., Topol, E. J., & Rajpurkar, P. (2023). Foundation models for generalist medical artificial intelligence. *Nature*, 616(7956), 259-265.
- [24] Chia, M. A., Antaki, F., Zhou, Y., Turner, A. W., Lee, A. Y., & Keane, P. A. (2024). Foundation models in ophthalmology. *British Journal of Ophthalmology*.
- [25] He, K., Chen, X., Xie, S., Li, Y., Dollár, P., & Girshick, R. (2022). Masked autoencoders are scalable vision learners. In *Proceedings of the IEEE/CVF conference on computer vision and pattern recognition* (pp. 16000-16009).
- [26] Iyer, N. S., Gulati, A., Banerjee, O., Logé, C., Farhat, M., Saenz, A. D., & Rajpurkar, P. (2022). Self-supervised pretraining enables high-performance chest X-ray interpretation across clinical distributions. *medRxiv*, 2022-11.

- [27] Huang, Z., Bianchi, F., Yuksekogonul, M., Montine, T. J., & Zou, J. (2023). A visual–language foundation model for pathology image analysis using medical twitter. *Nature medicine*, 29(9), 2307-2316.
- [28] Lu, M. Y., Chen, B., Williamson, D. F., Chen, R. J., Liang, I., Ding, T., ... & Mahmood, F. (2024). A visual-language foundation model for computational pathology. *Nature Medicine*, 30(3), 863-874.
- [29] Abbaspourazad, S., Elachqar, O., Miller, A. C., Emrani, S., Nallasamy, U., & Shapiro, I. (2023). Large-scale training of foundation models for wearable biosignals. *arXiv preprint arXiv:2312.05409*.
- [30] Pai, S., Bontempi, D., Hadzic, I., Prudente, V., Sokač, M., Chaunzwa, T. L., ... & Aerts, H. J. (2024). Foundation model for cancer imaging biomarkers. *Nature machine intelligence*, 6(3), 354-367.
- [31] Deng, J., Dong, W., Socher, R., Li, L. J., Li, K., & Fei-Fei, L. (2009, June). Imagenet: A large-scale hierarchical image database. In *2009 IEEE conference on computer vision and pattern recognition* (pp. 248-255). Ieee.
- [32] Strudel, R., Garcia, R., Laptev, I., & Schmid, C. (2021). Segmenter: Transformer for semantic segmentation. In *Proceedings of the IEEE/CVF international conference on computer vision* (pp. 7262-7272).
- [33] Hebert, H. L., Shepherd, B., Milburn, K., Veluchamy, A., Meng, W., Carr, F., ... & Palmer, C. N. (2018). Cohort profile: genetics of diabetes audit and research in Tayside Scotland (GoDARTS). *International journal of epidemiology*, 47(2), 380-381j.
- [34] Dosovitskiy, A., Beyer, L., Kolesnikov, A., Weissenborn, D., Zhai, X., Unterthiner, T., ... & Houlsby, N. (2020). An image is worth 16x16 words: Transformers for image recognition at scale. *arXiv preprint arXiv:2010.11929*.
- [35] Zhang, L., Wang, X., Yang, D., Sanford, T., Harmon, S., Turkbey, B., ... & Xu, Z. (2019). When unseen domain generalization is unnecessary? rethinking data augmentation. *arXiv preprint arXiv:1906.03347*.
- [36] Van der Maaten, L., & Hinton, G. (2008). Visualizing data using t-SNE. *Journal of machine learning research*, 9(11).
- [37] Simonyan, K., & Zisserman, A. (2014). Very deep convolutional networks for large-scale image recognition. *arXiv preprint arXiv:1409.1556*.
- [38] Loshchilov, I., & Hutter, F. (2016). Sgdr: Stochastic gradient descent with warm restarts. *arXiv preprint arXiv:1608.03983*.
- [39] Liu, L., Zhang, Z., Li, S., Ma, K., & Zheng, Y. (2021). S-CUDA: self-cleansing unsupervised domain adaptation for medical image segmentation. *Medical Image Analysis*, 74, 102214.
- [40] Lei, H., Liu, W., Xie, H., Zhao, B., Yue, G., & Lei, B. (2021). Unsupervised domain adaptation based image synthesis and feature alignment for joint optic disc and cup segmentation. *IEEE Journal of Biomedical and Health Informatics*, 26(1), 90-102.
- [41] Liu, B., Pan, D., Shuai, Z., & Song, H. (2022). ECSD-Net: A joint optic disc and cup segmentation and glaucoma classification network based on unsupervised domain adaptation. *Computer Methods and Programs in Biomedicine*, 213, 106530.
- [42] Chen, Z., Pan, Y., & Xia, Y. (2023). Reconstruction-driven dynamic refinement based unsupervised domain adaptation for joint optic disc and cup segmentation. *IEEE Journal of Biomedical and Health Informatics*, 27(7), 3537-3548.
- [43] Zhang, J., Lin, S., Cheng, T., Xu, Y., Lu, L., He, J., ... & Ma, Y. (2024). RETFound-enhanced community-based fundus disease screening: real-world evidence and decision curve analysis. *NPJ digital medicine*, 7(1), 108.
- [44] Power, A., Burda, Y., Edwards, H., Babuschkin, I., & Misra, V. (2022). Grokking: Generalization beyond overfitting on small algorithmic datasets. *arXiv preprint arXiv:2201.02177*.
- [45] Zhang, P., Li, Y., Zhang, J., Jiang, W., Conze, P. H., Lamard, M., ... & Daho, M. E. H. (2024, May). Detection and Classification of Glaucoma in the Justrags Challenge: Achievements in

- Binary and Multilabel Classification. In 2024 IEEE International Symposium on Biomedical Imaging (ISBI) (pp. 1-4). IEEE.
- [46] Du, K., Nair, A. R., Shah, S., Gadari, A., Vupparaboina, S. C., Bollepalli, S. C., ... & Vupparaboina, K. K. (2024). Detection of Disease Features on Retinal OCT Scans Using RETFound. *Bioengineering*, 11(12), 1186.
  - [47] Villaplana-Velasco, A., Pigeyre, M., Engelmann, J., Rawlik, K., Canela-Xandri, O., Tochel, C., ... & Bernabeu, M. O. (2023). Fine-mapping of retinal vascular complexity loci identifies Notch regulation as a shared mechanism with myocardial infarction outcomes. *Communications biology*, 6(1), 523.
  - [48] Wagner, S. K., Cortina-Borja, M., Silverstein, S. M., Zhou, Y., Romero-Bascones, D., Struyven, R. R., ... & Keane, P. A. (2023). Association between retinal features from multimodal imaging and schizophrenia. *JAMA psychiatry*, 80(5), 478-487.
  - [49] Mordi, I. R., Trucco, E., Syed, M. G., MacGillivray, T., Nar, A., Huang, Y., ... & Doney, A. S. (2022). Prediction of major adverse cardiovascular events from retinal, clinical, and genomic data in individuals with type 2 diabetes: a population cohort study. *Diabetes Care*, 45(3), 710-716.